

AperTO - Archivio Istituzionale Open Access dell'Università di Torino

Hidden soils and their carbon stocks at high-elevation in the European Alps (North-West Italy)

This is a pre print version of the following article:

Original Citation:

Availability:

This version is available <http://hdl.handle.net/2318/1763114> since 2023-11-22T15:30:46Z

Published version:

DOI:10.1016/j.catena.2020.105044

Terms of use:

Open Access

Anyone can freely access the full text of works made available as "Open Access". Works made available under a Creative Commons license can be used according to the terms and conditions of said license. Use of all other works requires consent of the right holder (author or publisher) if not exempted from copyright protection by the applicable law.

(Article begins on next page)

1 **Hidden soils and their carbon stocks at high-elevation in the European**

2 **Alps (North-West Italy)**

3
4 Emanuele Pintaldi¹, Michele E. D'Amico^{1*}, Nicola Colombo^{1,2,3}, Chiara Colombero⁴, Luigi
5 Sambuelli⁴, Claudio De Regibus⁴, Diego Franco⁴, Luigi Perotti³, Luca Paro⁵, Michele Freppaz^{1,2}

6
7 ¹University of Turin, Department of Agricultural, Forest and Food Sciences (DISAFA), Largo
8 Braccini, 2, 10095 Grugliasco (TO), Italy.

9 ²University of Turin, Research Center on Natural Risk in Mountain and Hilly Environments
10 (NatRisk), Largo Braccini, 2, 10095 Grugliasco (TO), Italy.

11 ³University of Turin, Department of Earth Sciences (DST), Via Valperga Caluso, 35, 10125 Turin,
12 Italy.

13 ⁴Politecnico di Torino, Department of Environment, Land and Infrastructure Engineering (DIATI),
14 Corso Duca degli Abruzzi, 24, 10129 Turin, Italy.

15 ⁵Regional Agency for Environmental Protection (Agenzia Regionale per la Protezione Ambientale -
16 ARPA) of Piedmont, Via Pio VII, 9, 10135 Turin, Italy.

17 18 **Abstract**

19 Alpine soils store large quantities of total organic carbon (TOC). Given their high sensitivity to
20 climate change, they may release large amounts of CO₂ in a warming climate scenario. Thus, it is
21 important to know their C stocks in order to estimate its possible release. While C stocks of forest,
22 dwarf shrub and alpine grassland soils are well documented, little is known about soils and C stocks
23 in high-elevated periglacial environments dominated by frost-driven processes. The object of this
24 study is the periglacial environment of the Stolenberg Plateau (LTER site Istituto Mosso, 3030 m
25 a.s.l.), at the foot of the Monte Rosa Massif (NW Italian Alps). The plateau is mostly covered by a

thick stony layer, organized in periglacial blockfields and blockstreams. The plant cover reaches only 3-5%. During the construction of a chair lift, open trenches revealed, unexpectedly, well-developed soils under the active periglacial stone cover. In particular, thick (30-65 cm) and dark TOC-rich A horizons were observed. Below these Umbric horizons, Cambic Bw ones were developed but discontinuous. Despite the lack of vegetation, C stocks were remarkably high (up to $\sim 5 \text{ kg m}^{-2}$), comparable to vegetated soils at lower elevation. Non-invasive geophysical methods revealed that these hidden soils were widespread on the plateau under the stony cover, with a mean thickness of around 50 cm. These TOC-rich soils, without vegetation and covered by periglacial landforms, represent a unique pedoenvironment suggesting new perspectives on the actual C-stocks at high-elevation sites, which are probably underestimated.

Keywords

Soil organic matter; Periglacial; Blockstream/Blockfield; Skeletic Umbrisol (Arenic, Turbic)

1 Introduction

Soil Organic Matter (SOM) stored in alpine soils (i.e. soils developed above the timberline, in alpine tundra and alpine desert, etc.) represents a considerable part of the global C cycle (e.g. Bockheim and Munroe, 2014), acting as a sink for carbon dioxide and having therefore a great potential to sequester this from the atmosphere (Bojko and Kabala, 2017). Alpine soils, especially those covered by vegetation and/or affected by permafrost, store large quantities of organic carbon (e.g. Celi et al., 2010; Bockheim and Munroe, 2014). However, given the high sensitivity of soils to climate change (Hagedorn et al., 2010a; Stanchi et al., 2015), they may release large amounts of carbon dioxide in a warming climate scenario (e.g. Hagedorn et al., 2010b; Schuur et al., 2013; Knowles et al., 2019). Generally, at high elevations in the European Alps, soils are mainly classified as Regosols, Cambisols, or Podzols (e.g. Egli et al., 2006; Zollinger et al., 2013; D'Amico et al.,

2020), often showing evidences of cryoturbation. In particular, high-elevation soils (i.e. above the alpine treeline) are affected by frost-action processes (e.g. frost-shattering, frost sorting, frost heave, solifluction etc.) (Karte, 1983), induced by seasonal frost penetration and/or permafrost (Van Vliet-Lanoë, 2014), leading to the formation of patterned ground, typical of periglacial environments (e.g. tilting of stones, blockstreams, blockfields, wedges, etc.) (e.g. Goodfellow, 2007; D'Amico et al., 2019). As these processes are mostly driven by temperature, active patterned ground is sensitive to climate warming, which can induce several effects such as permafrost degradation (e.g. Biskaborn et al., 2019; Mollaret et al., 2019), expansion of plant cover (e.g. Gerdol and Smiraglia, 1990), transition from pioneer species communities towards more acidophilous grassland (D'Amico et al., 2015), and increased SOM decomposition (e.g. Arteaga et al., 2008; Hagedorn et al., 2010a).

While the carbon stocks of forest and alpine grassland soils are well documented by several studies (e.g. Leifeld et al., 2009; Zollinger et al., 2013; Bockheim and Munroe, 2014), very little is known about carbon stocks in high-elevated periglacial environments, especially in the European Alps. This is probably due to different reasons, such as: 1) these soils are located in very unfavorable positions at high elevation and they are often difficult to reach, requiring specific technical equipment; 2) generally, these high-elevation areas are not covered by vegetation, therefore, as plants are the primary carbon source, these soils received less interest since they are not considered a relevant carbon sink compared to other soils; 3) high-elevation soils are often in periglacial environments, which are characterized by cryoturbation processes (induced by low temperatures and/or permafrost) that allow the formation of patterned ground and solifluction, which create an extreme spatial variability (D'Amico et al., 2015). They are frequently covered by coarse debris which makes it difficult to recognize them as soils and perform in-depth pedological investigations using manual devices.

In order to deepen the knowledge on these periglacial stone-covered environments, geophysical methods can be used thanks to their capability to map soil thickness even in areas with undulating topography, complex spatial distribution and non-homogeneous or anisotropic properties of the

77 investigated materials. Among the available geophysical methods, Electrical Resistivity
78 Tomography (ERT) allows investigating contrasts in electrical properties between the soil (loose,
79 porous, prone to water retention and possibly rich in organic matter) and massive bedrock or coarse
80 deposits. The same contrast in physical properties, together with differences in layering and other
81 internal structures, can be imaged using Ground Penetrating Radar (GPR) profiling. ERT and GPR
82 are widely used to support pedological surveys for soil characterization, mapping of the presence,
83 depth and lateral variability of soil horizons, agricultural purposes and contamination analyses from
84 low to mid latitudes and elevations (e.g. Samouelian et al., 2005; Allred et al., 2008; Doolittle and
85 Butnor, 2009; Andre et al., 2012; Nováková et al., 2013). By contrast, only few applications of
86 geophysical prospections for the study of high-elevation soils are reported in the literature (e.g.
87 Leopold et al., 2010; Pellet et al., 2016; Mollaret et al., 2019). In periglacial environments, these
88 techniques are mainly used for permafrost characterization, hydrogeological processes and loose
89 material-bedrock interface recognition (Moorman et al., 2003; Otto and Sass, 2006; Kneisel et al.,
90 2008; McClymont et al., 2010; Léger et al., 2017).

91 The research was performed in the severe periglacial environment of the Stolenberg Plateau on the
92 southern slope of Monte Rosa Massif (NW Italian Alps) where, in 2017, unexpected well-
93 developed soils within blockfields/blockstreams were found. Considering the impossibility to
94 deepen the investigation using manual devices and machinery, and the necessity to detect the
95 distribution of these hidden soils, non-invasive geophysical methods were applied in September
96 2019.

97 In this context, this work aims at: 1) describing and classifying the hidden soils, 2) determining
98 their carbon stock, and 3) investigating their local distribution and thickness, and potential
99 relationships with permafrost presence/distribution.

100

101 **2 Materials and methods**

102 **2.1 Study Area**

103 The work was carried out in the periglacial environment of the Stolenberg Plateau, a 13,500 m²
104 almost flat area located at 3030 m a.s.l., at the boundary between Valle d'Aosta and Piemonte
105 regions (Fig. 1a), at the foot of the southern slope of Monte Rosa (4634 m) (NW Italian Alps). The
106 study site represents the summit portion of the Long Term Ecological Research (LTER) site Angelo
107 Mosso Scientific Institute (LTER-Italia IT19-001-T), belonging to the LTER-Italy network. The
108 study area is also a Site of Community Importance and a Special Protection Area (SCI/SPA
109 IT1204220 "Ambienti glaciali del gruppo del Monte Rosa") (European Commission, 1992)
110 belonging to the Natura 2000 network.

111 From 2007 to 2018, the area had a mean annual air temperature of -2.2 °C, a mean cumulative
112 annual snowfall of 818 cm, and a mean annual liquid precipitation of ca. 400 mm. Snow cover lasts
113 for at least 8 months, reaching a maximum thickness of ca. 350 cm (Freppaz et al., 2019). In the
114 LTER-Italia IT19-001-T site, although at lower elevation and with alpine vegetation cover
115 (snowbed and grassland communities), soils were classified as Skeletic Dystric Regosol, Skeletic
116 Umbrisol, and Skeletic Dystric Cambisol (IUSS Working Group WRB, 2015) (Magnani et al.,
117 2017). Permafrost was detected at depths higher than 3-4 m on the nearby Corno del Camoscio
118 (3024 m a.s.l.) (Colombo et al., 2019). On the plateau, the slope steepness is below 10%, with large
119 flat portions in the central and eastern parts. The area shows typical features of periglacial
120 environments, characterized by active periglacial landforms. In particular, the plateau is covered by
121 a thick layer of stones with variable size (from decimeter to meter), well organized in blockfields,
122 blockstreams/sorted stripes, gelifluction lobes, tilted stones and weakly developed sorted circles
123 (Fig. 1b). In particular, blockstreams partly rearranged into sorted stripes are visible on sloping
124 surfaces, while blockfields, partly rearranged into patterned ground and rich in standing stones,
125 dominate the flatter surfaces. The activity of the periglacial processes is evidenced by the absence
126 of lichens from most stones (Ballantyne and Matthews, 1982). The parent material is composed of
127 gneiss and mica-schists (Monte Rosa nappe, Penninic basement) and metabasites (Zermatt-Saas
128 unit) (Mattiolo et al., 1951). No traces of glacial till are observed, as all blocks seem autochthonous

129 (Ballantyne, 2010; Goodfellow, 2007); the best developed blockstreams are located around rock
130 outcrops, and are clearly derived by their cryofracturation. The glacial history of the plateau is
131 currently unknown.

132 The vegetation cover, which is extremely scarce and confined to small patches reaching no more
133 than 5% of the plateau areal extension, is composed mainly of alpine and nival species such as
134 *Silene acaulis*, *Carex curvula*, *Salix herbacea* in the vegetated patches, while *Festuca halleri*, *Poa*
135 *alpina*, *Ranunculus glacialis*, *Leuchanemopsis alpina*, *Cerastium uniflorum* and a few other
136 pioneer species grow also in the stone-covered area, with extremely low cover values. A higher
137 vegetation cover characterizes a small area in the northern side, close to the edge of the cliff, on
138 slightly more weatherable amphibolites.

139

140 **2.2 Soil survey, sampling and analysis**

141 In 2017, during the operational activities for the construction of a new chair lift, the largest part of
142 the plateau was delimited in order to protect the natural environment (Directive, 1992) and the
143 periglacial features against the excavation operations. However, three trenches were opened (2 to 10
144 m long, to a depth of around 1.2 m) in the construction area, revealing unexpected, well-developed
145 soils under the stony cover. This finding was possible only thanks to the machinery employed,
146 whose utilization was exceptionally allowed for the construction of the chair lift station.

147 Field description of soil transects was performed according to FAO (2006), while soil classification
148 was done according to WRB classification system (IUSS Working Group WRB, 2015). The three
149 trenches (soil profiles) were described and sampled (Fig. 1a). Each profile was subdivided into
150 sectors characterized by a similar sequence of horizons. Overall, 27 soil samples were collected
151 from all genetic horizons in the profiles; at least one sample per genetic horizon was sampled in
152 each sector (ca. 300-500 g per sample). The samples were air-dried, sieved to 2 mm and analyzed
153 following the standard methods reported by Van Reeuwijk (2002). The pH was measured in soil-
154 water suspension (soil:water = 1:2.5). The particle-size analysis was performed by the pipette

method after organic matter destruction with H₂O₂ followed by dispersion with Na-hexametaphosphate. Total carbon (corresponding to total organic carbon-TOC due to the absence of carbonates) and nitrogen (TN) concentrations, were measured by dry combustion with an elemental analyzer (CE Instruments NA2100, Rodano, Italy).

The soil organic carbon stock (C-STOCK_{tot} kg m⁻²) of the profiles was calculated for sectors in which the horizons sequence was similar, according to the following equation adapted from Batjes (1996):

$$C - STOCK_{tot} = \sum_{i=1}^n \frac{TOC * BD * TH * VF}{1000} \quad (1)$$

where n is the number of soil horizons of each sector, TOC is the soil organic carbon concentration (g kg⁻¹) of the mineral horizons, BD is the Bulk Density (kg m⁻³) based on mean Bulk Density values of high-elevation soils (D'Amico et al., still unpublished) measured according to Boone et al. (1999), TH is the horizon thickness (m), VF is the volume of fine earth excluding the coarse mineral fraction (> 2 mm, visually estimated in the field (%) for each horizons), calculated as [1 – (% rock volume/100)], 1000 is the unit correction factor.

In order to support the interpretation of the geophysical measurements, the clay minerals were analyzed using a Philips PW1710 X-ray diffractometer (40kV and 20 mA, CoK α radiation, graphite monochromator). The Mg saturated clay fraction (< 2 μ m) was separated by sedimentation, flocculated with MgCl₂, washed until free of Cl⁻, and freeze-dried. Scans were made from 3 to 35 $^{\circ}$ 2 θ at a speed of 1 $^{\circ}$ 2 θ min⁻¹, on air dried, ethylene glycol solvated, and heated (350 $^{\circ}$ and 550 $^{\circ}$ C) oriented mounts. A semi-quantitative evaluation of mineral abundance was performed using the Mineral Intensity Factors method (Islam and Lotse, 1986), which considers peak areas. For the calculation, the background was subtracted and the peak positions, intensities and areas were calculated using the PowderX software (Dong, 1999).

178

2.3 Geophysical investigation

180 Six 48-electrode Electrical Resistivity Tomography (ERT) profiles were acquired (Fig. 1a). Five of
181 them had an inter-electrode spacing of 0.30 m, for a total length of 14.1 m. One longer profile (ERT
182 3 in Fig. 1a) was acquired with a spacing of 2 m between the electrodes, for a total length of 94 m.
183 With the short profiles we aimed at the detection and lateral imaging at shallow depths of the buried
184 soils with high-resolution, while the longer line was designed for a deeper general low-resolution
185 characterization of the bedrock conditions below the soil horizons. To constrain data interpretation,
186 reference values for the soil electrical resistivity were derived from the statistical analysis of
187 measurements carried out in an uncovered soil outcrop (approximately 1.5 x 0.3 m) with a single
188 quadrupole (0.25-, 0.30- and 0.40-m electrode spacing, eight array configurations of current and
189 potential electrode positions).

190 ERT electrodes were georeferenced using a Garmin GPS 60 system to overlay the position of each
191 survey line on a high-resolution digital surface model (DSM) of the plateau and later account for the
192 significant topographic variations in the inversion of the longest ERT line. Digital vertical and
193 slantwise photos obtained from an Unmanned Aerial Vehicle (UAV) survey were processed with
194 structure from motion and multi-view-stereo algorithms to produce a high-resolution DSM (10 cm /
195 pixel ground resolution) of the investigated area (e.g. Smith et al., 2015; Carrivick et al., 2016,
196 Alberto et al., 2018) (Supplementary Material, SM1).

197 Ten ground penetrating radar (GPR) profiles (Fig. 1a) were complementary acquired with a 500-
198 MHz antenna controlled by an IDS K2 digital acquisition unit. GPR traces were acquired for a total
199 time of 100 ns and 512 samples per trace. Ublox EVK-5T GPS was used to track each survey
200 position. The average distance between subsequent traces resulted in 0.025 m along each line.

201 Local rare diffraction hyperbola in the processed radargrams were fitted with a velocity of 0.1 m/ns.
202 To apply this value for time-to-depth conversion, the medium velocity (v) was additionally
203 estimated by the Complex Refractive Index Method (CRIM, Birchak et al., 1974; Wharton et al.,
204 1980), following:

$$205 \quad \sqrt{\varepsilon_s} = (1 - \varphi) \sqrt{\varepsilon_m} + \varphi S \sqrt{\varepsilon_w} + \varphi (1 - S) \sqrt{\varepsilon_a} \quad (2)$$

206 and

$$207 \quad v = \frac{c}{\sqrt{\epsilon_s}} \quad (3)$$

208 where ϵ_s , ϵ_m , ϵ_w and ϵ_a are the relative dielectric permittivities of soil (solid matrix + pore space),
209 solid matrix, pore water and air respectively, ϕ is the soil porosity, S is the degree of water
210 saturation and c is the electromagnetic wave velocity in vacuum ($3 \cdot 10^8$ m/s). In Equation 2, $\epsilon_a=1$,
211 $\epsilon_w=77.8$ (from GPR measurements on the water of a nearby pond; Colombo et al., 2018) and $\epsilon_m=7$
212 (from average reference values of similar loamy sandy soils, e.g. Daniels, 2004). Soil porosity ϕ
213 was indirectly estimated from density measurements in the range 0.5 to 0.6. Moist (unsaturated)
214 conditions were present on site during GPR acquisitions. A variable S , between 0.2 and 0.4, was
215 consequently considered in the computation. Using these parameters, average $\epsilon_s=9.3$ and $v=0.10$
216 m/ns were obtained for time-to-depth conversion. The approximate wavelength of a 500-MHz GPR
217 signal in this material is consequently 0.2 m, meaning approximately 0.1 m of vertical resolution
218 (half wavelength) in the investigated medium.

219 Additional details on ERT and GPR processing are given in Supplementary Material SM2.

220

221 **2.4. Bottom temperature of snow cover and ground temperature**

222 To investigate the ground surface thermal conditions in the investigated area, the bottom
223 temperature of the snow cover (BTS, e.g. Hoelzle, 1992) measurements were performed in 2014,
224 2015, and 2019. To acquire BTS data, a thermometer Delta Ohm RTD HD 2307.0 (accuracy ± 0.05
225 $^{\circ}\text{C}$, resolution 0.1 $^{\circ}\text{C}$), equipped with a probe Pt100 TP474C.0, was installed on a stainless steel
226 probe. The location of each sample point was recorded with a handheld Global Positioning System
227 (GPS) ("Aventura" TwoNav vs. 2.6.2). The measurements were performed during the late winter
228 (March/April), when a sufficient snow cover was established since at least one month, before the
229 onset of snow melt. Since a minimum snow thickness of 80 cm is necessary to provide a sufficient

230 insulation against air temperature variations, measurements were made only where this threshold
231 was found, obtaining about 260 measurements.

232 Ground temperature (GT) data from a 5-m deep borehole managed by Arpa Piemonte in the north-
233 eastern side of the plateau were also used to analyse the ground thermal conditions. Daily data from
234 04 November 2017 to 29 July 2019 were analysed; no data gaps were present in the series.

235

236 **3 Results**

237 **3.1. Soil profiles characteristics**

238 The stony/blocky layer (blockfields and blockstreams, respectively on flat surfaces or on gentle
239 slopes) was 10-60 cm thick, and it was usually well graded with depth, with the coarsest stones on
240 the surface and fine ones at the bottom, associated with A1 horizons, as typically observed in
241 blockfields and blockstreams (Wilson, 2013). Below the stone layer, the profiles were characterized
242 by thick (between 30 and 65 cm) and continuous, dark A and A@ horizons with subangular-blocky,
243 platy or granular structure (Table 1, Figs. 2, 3 and 4). These horizons were characterized by few
244 living or dead roots and very few, extremely weak, isolated, biogenic fine granular aggregates. They
245 were classified as Umbric horizons according to WRB (IUSS Working Group WRB, 2015). In fact,
246 the diagnostic criteria for Umbric horizons, calculated in the top 20 cm, are dark colors (moist
247 chroma and value ≤ 3), darker colors than the horizons underlying it or the parent material, soft or
248 friable consistence and not massive structure, $\geq 0.6\%$ TOC, $\text{pH} < 5.5$ or base status $< 50\%$. Below
249 the Umbric horizons, Cambic Bw ones were often developed although discontinuous, characterized
250 by brown color and well-developed subangular-blocky structure (Table 1, Figs. 2, 3 and 4). Stones
251 were quite scarce, particularly in A horizons, evidencing frost sorting and cryoexpulsion. The stones
252 were moderately weathered and were quite easily broken with a spade, particularly in Bw horizons,
253 while they were weakly weathered in the surface layer. Cryoturbation features, such as inclusions of
254 surface A materials at depth (horizons n. 7 in Fig. 3) as well as convolutions and block

displacement above wedges, were often observed within the profiles. In profile 3, blocks shown as “a” in Fig. 2 were dislocated and raised by freeze-thaw processes from the rock layer evidenced by letters “b” and “c”, above a deep fracture (wedge). Thick, dense silt caps were also observed on the upper faces of stone fragments. Below the Bw, BC and CB horizons, the highly fractured bedrock was always observed. The soils were classified as Skeletic Umbrisol (Arenic, Turbic), according to IUSS Working Group WRB (2015).

261

3.2 Soils physical and chemical properties

The soil texture of all horizons was generally loamy sand or sandy loam, with a substantial prevalence of sand (77% on average) compared to silt (20%) and clay (3%) fractions (Tab. 1). The clay fraction was composed of ca. 60% quartz, 20% mica/illite, 10% chlorite, 10% plagioclase and other minerals in traces (not shown), reflecting a similar mineralogy as the parent material. pH values were extremely to moderately acidic, ranging between 4.3 and 5.9. TOC content spanned from 0 to over 2%, reaching maximum values in A horizons, while TN values were very low in all the samples. The TOC/TN ratio ranged between 7 and 20, reaching maximum values in the A horizons.

Considering the overall C-STOCK_{tot} of each sector within the profiles (Table 2, Figs. 2, 3 and 4), in P1 the values ranged between 0.7 and over 5 kg m⁻², reaching minimum and maximum values in sector C and A respectively; in the profile P2 the values spanned from 1.12 to approx. 3 kg m⁻² reaching minimum values in sector D and maximum in sector F; the C-STOCK_{tot} of P3 reached the minimum value of 2.17 kg m⁻² in sector K and a maximum of 3.30 in kg m⁻² in the sector I.

276

3.3 Geophysical investigation

Results obtained from the long ERT line (ERT3 in Fig. 5a) provided a non-homogeneous electrical resistivity distribution in the plateau bedrock. The deepest values (6-8 kΩ m in the line center below

280 5-m depth, yellow in Fig. 5a) were interpreted as representative of compact bedrock. Higher
281 resistivities ($>8 \text{ k}\Omega \text{ m}$, green in Fig. 5a) were depicted at shallower depths, reaching values of 50
282 $\text{k}\Omega \text{ m}$ in proximity of the fractured overhanging rock cliff delimiting the plateau eastern edge.
283 These values were related to variable fracturing conditions of the shallow bedrock, increasing
284 towards E and NE. An isolated high-resistivity area ($> 75 \text{ k}\Omega \text{ m}$) was found at approx. 2 m depth
285 towards the E-NE section of the ERT3 (Fig. 5a).

286 Above the fractured bedrock, all the short ERT lines revealed the presence of a distinct and
287 discontinuous layer with variable thickness under the stony cover, with resistivity values lower than
288 $6 \text{ k}\Omega \text{ m}$ (orange to red in Fig. 5, b to d). Separated measurements acquired on an uncovered soil
289 outcrop showed resistivity values in the range 2.9-4.2 $\text{k}\Omega \text{ m}$, with an average of 3.6 $\text{k}\Omega \text{ m}$ over 24
290 tests with different array spacing and electrode configuration. Consequently, this shallow layer was
291 interpreted as representative of the soil presence under the periglacial cover.

292 The GPR profiles depicted a complex stratigraphy in the first meters of depth. Exemplificative
293 results are illustrated in Fig. 6 for the GPR profiles acquired along the ERT lines of Fig. 5.
294 Processed radargrams were visually interpreted as shown in Fig. 6a. In the shallowest part of each
295 section, GPR reflections appear as laterally continuous, smooth and sub-horizontal, likely due to the
296 soil presence (s in Fig. 6a). Below this layer, intricate patterns of discontinuous GPR reflections are
297 conversely present, more steeply dipping in different directions. This layer (t in Fig. 6a) possibly
298 corresponds to the transition between soil and bedrock. The chaotic arrangement of soil material
299 and debris resulting from the fractured bedrock may have generated this complex GPR response. At
300 depths higher than 1 m, GPR reflections show again a more homogeneous lateral continuity,
301 possibly indicating the bedrock presence (b in Fig. 6a).

302 Given the difficulty and subjectivity in manually picking the soil bottom basis from GPR sections
303 (Fig. 6, b, d and f), ERT results (Fig. 5) were transformed in total gradient sections of electrical
304 resistivities. The gradient maxima in each section were then automatically picked and interpreted as
305 objective markers of the presence of a sharp vertical and lateral contrast between soil and

306 surrounding materials and consequently used to estimate the average soil thickness in the plateau.
307 Results are shown in Fig. 6 (c, e and g) in comparison with manual picking performed on GPR
308 sections. Electrical resistivity gradient maxima generally fall within the transition layer (Fig. 6a)
309 depicted in GPR results, providing a rough estimate of the soil-substrate interface.
310 The soil presence was detected by both geophysical methods within the first meter of depth of all
311 the investigated lines.
312

313 **3.4 Ground temperature conditions (BTS and GT)**

314 The BTS measurements highlighted a thermal difference between the northern and the southern side
315 of the plateau. Colder ground surface temperatures (often below -2/-3 °C) in the southern portion of
316 the plateau gradually became warmer (generally above -2/-1 °C) towards the northern zone, where
317 only few spots highlighted temperature below -2/-3 °C (Fig. 7a). In additions, a clear
318 correspondence between a cold BTS spot and a high resistivity body detected by the long ERT3 was
319 found (Fig. 7a). Regarding the borehole, maximum GTs reached decisively positive values at all
320 depths during the investigated period (Fig. 7b).
321

322 **4 Discussion**

323 **4.1 Soil properties and carbon stocks**

324 The opening of trenches revealed the unexpected presence of complex and well-developed soils
325 (Umbrisols) under the stony cover, with convolutions and inclusions of different materials, as a
326 result of intense cryoturbation processes as described by Bockheim and Tarnocai (1998) in
327 permafrost-affected soils. Despite the strong geomorphic activity characterizing this periglacial
328 area, the observed soils were extremely well developed, particularly inside periglacial landforms
329 (blockfields and blockstreams). Considering the remarkable thickness of A horizons (up to 60 cm),
330 these soils are considerably more developed than the surrounding soils with or without vegetation,

331 at similar or lower elevation, where weakly developed and shallow Skeletic Regosols, Cambisols or
332 Umbrisols (e.g. Magnani et al., 2017) with thinner A horizon (up to 25-30 cm) were common.
333 Nevertheless, the textural class as well as the pH values were comparable to those found in the
334 surrounding soils under snowbed vegetation (e.g. Magnani et al., 2017). In the Italian Alps, very
335 few works reported soils with C-rich A horizons at high elevation (around 3000 m a.s.l.), for
336 instance Baroni and Orombelli (1996) describe Inceptisols with C-rich A horizons at the Tisa Pass
337 (~ 3200 m a.s.l, Eastern Alps, close to the Italian-Austrian border), although thinner and less
338 developed compared to our soils.

339 Considering the absence of a significant vegetation cover on the plateau and the high elevation, the
340 estimated total carbon stock for each sector was surprisingly high. Overall, the carbon stocks were
341 comparable to the ones reported for high-elevation, cryoturbated soils in the Aosta Valley, although
342 generally covered by alpine tundra, for which values around 2-3 kg m⁻² (D'Amico et al., still
343 unpublished) were calculated. The values were also in the range reported for other vegetated soils in
344 Alpine tundra ecosystems (Bockheim and Munroe, 2014). Moreover, our results, in particular from
345 soil profile P1, despite the lack of vegetation, were also in the normal range of carbon stock values
346 from moderately developed forest or heath soils in the Aosta Valley, such as Entic Podzols
347 (D'Amico et al., 2020), and to those reported by Chiti et al. (2012) for forest ecosystems in Spain,
348 for mountain boreal forests in North America (Hoffmann et al., 2014) or for mountain soils in the
349 Veneto region (North-East Italian Alps) (Garlato et al., 2009).

350

351 **4.2 Soil distribution, depth and subsurface morphology of the plateau**

352 Geophysical investigations confirmed the widespread presence of soils on the whole plateau.
353 Considering the soil texture, the measured electrical resistivity values (up to 6 kΩ m) may appear
354 unusually high for field tests carried out in moist (but unsaturated) conditions on these materials.
355 Since the proportion of minerals having relevant surface conductivity was found to be almost

negligible (i.e. illite and chlorite are less than 1% of the total solid matrix), a rough check on the expected soil electrical resistivity ρ_s can be performed following Archie's law (Archie, 1942):

$$\rho_s = a \frac{\rho_w}{\varphi^m S^k} \quad (4)$$

where ρ_w is pore water resistivity (around 100 Ω m, i.e. moisture mainly due to precipitation and shallow seepage), $a=1$ and $m=1.4$ are Archie's coefficients for non-consolidated sediments (Archie, 1942; Friedman, 2005), φ is the soil porosity (0.5 to 0.6), S is the degree of water saturation and k coefficient can be assumed equal to 2 for $S>0.1$. Applying Equation 4, retrieved ρ_s values are in the range 1.3-6.5 k Ω m for S between 0.2 and 0.4, thus additionally confirming the obtained electrical resistivity values.

Thanks to the electrical resistivity gradient maxima analyses, the soil-substrate interface was recognized at depths ranging from 26 to 88 cm, for an average of 47 cm over the five short ERT lines. In general, higher depths (and soil thicknesses) were identified in the eastern part of the plateau (ERT2, ERT5 in Fig. 1a), close to the chair lift station, in presence of a more fractured underlying bedrock and below a particularly coarse stone cover. By contrast, the lowest depths were found in the grassy area on the northern side of the plateau, where periglacial blockfields/blockstreams are absent (ERT6 in Fig. 1a). A decrease in soil thickness was also observed close to the rock outcrops present in the plateau. Even if ERT surveys had lower vertical resolution with respect to GPR profiles, soil depth and thickness estimations from electrical resistivity gradient maxima were straightforward and provided a less subjective estimation in these complex subsurface settings.

Regarding the potential permafrost presence and distribution, relatively low electrical resistivity values pointed towards the absence of relevant bodies of permafrost in the investigated area (e.g. Kneisel, 2006), also considering the lithology of the bedrock and its fracturing conditions. This is in agreement with the BTS values, which indicated higher likelihood of permafrost presence in the southern portion of the plateau, while in the northern portion (where we performed our investigations) generally warmer values suggested only the potential presence of sporadic

382 permafrost (cf., Julián and Chueca, 2007). Interestingly, a correspondence between a cold BTS spot
383 and a high resistivity body was found. In this spot, we hypothesize the presence of a body of
384 isolated permafrost, which is in agreement with its local setting. Further confirmation of the current
385 mostly permafrost-free conditions of the area derived from the GT data, which evidenced the
386 absence of permafrost at all depths at the borehole site and relatively warm winter temperatures.
387 Considering the remarkable thickness of the soil layer (particularly where periglacial features are
388 thicker) and its general wide distribution, we assume that the overall C-stock of the plateau may be
389 higher. In particular, the southern and south-western portions of the plateau (impossible to
390 investigate except by means of heavy machinery) are covered by a particularly coarse and thick
391 block cover, which resembles the eastern part where the soil thickness and C stocks are larger. In
392 this area, like in the one overlying the high-resistivity body along the ERT3, the coarse stones thus
393 protect soil C and permafrost conditions at depth as well.

394

395 **5 Conclusion and perspectives**

396 During the operational activities for a new chair lift construction at the Stolenberg Plateau, the
397 opening of soil trenches revealed, unexpectedly, the presence of extremely well-developed soils
398 under a thick stony cover consisting of periglacial blockfields and blockstreams. These soils,
399 classified as Umbrisol, were characterized by surprisingly high C stocks, comparable to alpine
400 tundra or even forest soils, despite the lack of vegetation and the presence of the stony cover. The
401 application of non-invasive geophysical methods revealed that these hidden soils were widespread
402 on the plateau under the stony cover, with a mean thickness of around 50 cm, that generally
403 increase (up to ca. 90 cm) where the periglacial blockfields/blockstreams were thickest.
404 These C-rich soils, without vegetation and hidden inside periglacial landforms, may represent a
405 unique pedoenvironment suggesting new perspective on the actual C stocks in high-elevation
406 environment, which are probably underestimated. Since the origin of these C-rich soils inside
407 blockstreams and blockfields is apparently in contrast with present day condition, these findings

408 may be of great relevance for unravelling the history of the high-elevation landscape of the Monte
409 Rosa area. For instance, if these soils represent buried paleosols below moving stone layers, they
410 might retain information about past climate. Alternatively, in order to explain the high organic
411 matter content below the stone cover considering recent conditions, it may be argued that
412 decomposition rates are extremely low as a result of the cooling effect of the stone cover. To clear
413 up those unresolved questions, a more precise characterization of the organic matter, its age and
414 plant remains has to be performed by further studies in the area.

415

416 **Acknowledgements**

417 This study was supported by European Regional Development Fund in Interreg Alpine Space
418 project Links4Soils (ASP399): Caring for Soil—Where Our Roots Grow. ([http://www.alpinespace.](http://www.alpinespace.eu/projects/links4soils/en/the-project)
419 [eu/projects/links4soils/en/the-project](http://www.alpinespace.eu/projects/links4soils/en/the-project)). Many thanks to Monterosa Ski Resort (project stakeholder)
420 for providing logistical support.

421 **References**

- 422 Alberto, W., Palomba, M., Perotti, L., 2018. SMART GROUND project test-sites topographic and
423 morphologic characterization: Instruments and methodologies. *Rendiconti Online Società Geologica*
424 Italiana 46, 107–114. <https://doi.org/10.3301/ROL.2018.60>
- 425 Allred B.J., Daniels J.J., Ehsani M.R., 2008. *Handbook of Agricultural Geophysics*. CRC Press Taylor Francis
426 Group, Boca Raton. <https://doi.org/10.1201/9781420019353>
- 427 Andre F., van Leeuwen C., Saussez S., van Durmen R., Bogaert P., Moghadas D., de Resseguier L., Delvaux B.,
428 Vereecken H.; Lambot S., 2012. High-resolution imaging of a vineyard in south of France using ground
429 penetrating radar, electromagnetic induction and electrical resistivity tomography. *Journal of Applied*
430 Geophysics, 78, 113–122. <https://doi.org/10.1016/j.jappgeo.2011.08.002>
- 431 Archie, G.E., 1942. The electrical resistivity log as an aid in determining some reservoir characteristics.
432 *Trans. Am. Inst. Mech. Eng.* 146, 54–67. <https://doi.org/10.2118/942054-G>
- 433 Arteaga, G.Á., Calderón, N.G., Krasilnikov, P.V., Sedov, S.N., Targulian, V.O., Rosas, N.V., 2008. Soil
434 altitudinal sequence on base-poor parent material in a montane cloud forest in Sierra Juárez,
435 Southern Mexico. *Geoderma* 144, 593–612. <https://doi.org/10.1016/j.geoderma.2008.01.025>
- 436 Ballantyne, C.K., Matthews, J.A., 1982. The development of sorted circles on recently deglaciated terrain,
437 Jotunheimen, Norway. *Arctic and Alpine Research* 14, 341–354.
438 <https://doi.org/10.1080/00040851.1982.12004316>
- 439 Ballantyne, C. K. (2010). A general model of autochthonous blockfield evolution. *Permafrost and Periglacial*
440 Processes, 21(4), 289-300. <https://doi.org/10.1002/ppp.700>
- 441 Baroni, C., Orombelli, G., 1996. The Alpine “Iceman” and Holocene Climatic Change. *Quat. res.* 46, 78–83.
442 <https://doi.org/10.1006/qres.1996.0046>
- 443 Batjes, N.H., 1996. Total carbon and nitrogen in the soils of the world. *Eur J Soil Science* 47, 151–163.
444 <https://doi.org/10.1111/j.1365-2389.1996.tb01386.x>
- 445 Birchak, J.R., Gardner, C.G., Hipp, J.E., and Victor, J.M., 1974. High dielectric constant microwave probes for
446 sensing soil moisture: *Proc. IEEE*, 62, 93-98. DOI: 10.1109/PROC.1974.9388
- 447 Biskaborn, B.K., Smith, S.L., Noetzli, J., Matthes, H., Vieira, G., Streletskiy, D.A., Schoeneich, P., Romanovsky,
448 V.E., Lewkowicz, A.G., Abramov, A., Allard, M., Boike, J., Cable, W.L., Christiansen, H.H., Delaloye, R.,
449 Diekmann, B., Drozdov, D., Etzelmüller, B., Grosse, G., Guglielmin, M., Ingeman-Nielsen, T., Isaksen,
450 K., Ishikawa, M., Johansson, M., Johannsson, H., Joo, A., Kaverin, D., Kholodov, A., Konstantinov, P.,
451 Kröger, T., Lambiel, C., Lanckman, J.-P., Luo, D., Malkova, G., Meiklejohn, I., Moskalenko, N., Oliva,
452 M., Phillips, M., Ramos, M., Sannel, A.B.K., Sergeev, D., Seybold, C., Skryabin, P., Vasiliev, A., Wu, Q.,
453 Yoshikawa, K., Zheleznyak, M., Lantuit, H., 2019. Permafrost is warming at a global scale. *Nat*
454 *Commun* 10, 264. <https://doi.org/10.1038/s41467-018-08240-4>
- 455 Bockheim, J.G., Munroe, J.S., 2014. Organic Carbon Pools and Genesis of Alpine Soils with Permafrost: A
456 Review. *Arctic, Antarctic, and Alpine Research* 46, 987–1006. [https://doi.org/10.1657/1938-4246-](https://doi.org/10.1657/1938-4246-46.4.987)
457 [46.4.987](https://doi.org/10.1657/1938-4246-46.4.987)
- 458 Bockheim, J.G., Tarnocai, C., 1998. Recognition of cryoturbation for classifying permafrost-affected soils.
459 *Geoderma* 81, 281–293. [https://doi.org/10.1016/S0016-7061\(97\)00115-8](https://doi.org/10.1016/S0016-7061(97)00115-8)
- 460 Bojko, O., Kabala, C., 2017. Organic carbon pools in mountain soils — Sources of variability and predicted
461 changes in relation to climate and land use changes. *CATENA* 149, 209–220.
462 <https://doi.org/10.1016/j.catena.2016.09.022>
- 463 Boone R.D., Grigal D.F., Sollins P., Ahrens R.J., Armstring, D.E., 1999. Soil sampling, preparation, archiving,
464 and quality control. In: Robertson G.P., Coleman D.C., Bledsoe C.S., Sollins P., (eds) *Standard soil*
465 *methods for long-termecological research*. Oxford University Press, New York, pp 3–28.
- 466 Carrivick, J.L., Smith, M.W., Quincey, D.J., 2016. *Structure from Motion in the Geosciences*. John Wiley &
467 Sons, Ltd, Chichester, UK. <https://doi.org/10.1111/phor.12173>
- 468 Celi, L., Rosso, F., Freppaz, M., Agnelli, A., Zanini, E., 2010. Soil Organic Matter Characteristics in Sporadic
469 Permafrost-affected Environment (Creux du Van, Switzerland). *Arctic, Antarctic, and Alpine Research*
470 42, 1–8. <https://doi.org/10.1657/1938-4246-42.1.1>
- 471

472 Chiti, T., Díaz-Pinés, E., Rubio, A., 2012. Soil organic carbon stocks of conifers, broadleaf and evergreen
473 broadleaf forests of Spain. *Biology and Fertility of Soils*, 48(7), 817-826. DOI 10.1007/s00374-012-
474 0676-3

475 Colombo, N., Sambuelli L., Comina C., Colombero C., Giardino M., Gruber, S., Viviano, G., Vittori Antisari, L.,
476 Salerno, F., 2018. Mechanisms linking active rock glaciers and impounded surface water formation in
477 high-mountain areas. *Earth Surface Processes and Landforms*, 43(2), 417-431. DOI: 10.1002/esp.4257

478 Colombo, N., Salerno, F., Martin, M., Malandrino, M., Giardino, M., Serra, E., Godone, D., Said-Pullicino, D.,
479 Fratianni, S., Paro, L., Tartari, G., Freppaz, M., 2019. Influence of permafrost, rock and ice glaciers on
480 chemistry of high-elevation ponds (NW Italian Alps). *Science of The Total Environment*, 685, 886-901.
481 <https://doi.org/10.1016/j.scitotenv.2019.06.233>

482 D'Amico, M., Gorra, R., Freppaz, M., 2015. Small-scale variability of soil properties and soil-vegetation
483 relationships in patterned ground on different lithologies (NW Italian Alps). *CATENA* 135, 47–58.
484 <https://doi.org/10.1016/j.catena.2015.07.005>

485 D'Amico, M.E., Pintaldi, E., Catoni, M., Freppaz, M., Bonifacio, E., 2019. Pleistocene periglacial imprinting on
486 polygenetic soils and paleosols in the SW Italian Alps. *Catena*, 174, 269-284.
487 <https://doi.org/10.1016/j.catena.2018.11.019>

488 D'Amico, M.E., Pintaldi, E., Sapino, E., Colombo, N., Quaglino, E., Stanchi, S., Navillod, E., Rocco, R., Freppaz,
489 M., 2020. Soil Types of the Aosta Valley (NW Italy). *J. Maps*.
490 <https://doi.org/10.1080/17445647.2020.1821803>

491 Daniels, D.J., 2004. Ground Penetrating Radar. 2nd edition. Radar, Sonar, Navigation and Avionics Series 15,
492 Institute of Electrical Engineers, London, UK. DOI: 10.1049/PBRA015E

493 Dong, C., 1999. PowderX: Windows-95 based program for powderX-ray diffraction data processing. *J Appl*
494 *Crystallogr.* 32, 838. <https://doi.org/10.1107/S0021889899003039>

495 Doolittle, J.A., Collins M.E., 1995. Use of soil information to determine application of ground penetrating
496 radar. *Journal of Applied Geophysics*, 33, 101–108. [https://doi.org/10.1016/0926-9851\(95\)90033-0](https://doi.org/10.1016/0926-9851(95)90033-0)

497 Egli, M., Mirabella, A., Sartori, G., Zanelli, R., and Bischof, S., 2006: Effect of north and south exposure on
498 weathering rates and clay mineral formation in alpine soils. *Catena*, 67, 155–174.
499 <https://doi.org/10.1016/j.catena.2006.02.010>

500 European Commission, 1992. Council Directive 92/43/EEC of 21 May 1992 on the conservation of natural
501 habitats and of wild fauna and flora. *Official Journal of the European Union* 206, 7–50.
502 <http://data.europa.eu/eli/dir/1992/43/oj>

503 FAO, 2006. Guidelines for soil description, 4th ed., 2006. Food and Agriculture Organization of the United
504 Nations, Rome. ISBN 92-5-105521-1

505 Freppaz, M., Viglietti, D., Balestrini, R., Lonati, M., Colombo, N., 2019. Climatic and pedoclimatic factors
506 driving C and N dynamics in soil and surface water in the alpine tundra (NW-Italian Alps). *NC* 34, 67–
507 90. <https://doi.org/10.3897/natureconservation.34.30737>

508 Friedman, S.P., 2005. Soil properties influencing apparent electrical conductivity: a review. *Comput.*
509 *Electron. Agric.* 46, 45–70. <https://doi.org/10.1016/j.compag.2004.11.001>

510 Garlato, A., Obber, S., Vinci, I., Sartori, G., Manni, G., 2009. Stock attuale di carbonio organico nei suoli di
511 montagna del Veneto. *Studi Trentini di Scienze Naturali. Suoli degli ambienti alpini* 85, 69–82. ISSN
512 203 5-7 699

513 Gerdol, R., Smiraglia, C., 1990. Correlation between vegetation pattern and microtopography in periglacial
514 areas of the Central Alps. *Pirineos* 135, 13–28. <https://doi.org/10.3989/pirineos.1990.v135.208>

515 Goodfellow, B. W., 2007. Relict non-glacial surfaces in formerly glaciated landscapes. *Earth-Science*
516 *Reviews*, 80(1-2), 47-73.

517 Hagedorn, F., Mulder, J., Jandl, R., 2010a. Mountain soils under a changing climate and land-use.
518 *Biogeochemistry*, 97(1), 1-5. DOI: 10.1007/s10533-009-9386-9

519 Hagedorn, F., Martin, M., Rixen, C. et al., 2010b. Short-term responses of ecosystem carbon fluxes to
520 experimental soil warming at the Swiss alpine treeline. *Biogeochemistry* 97, 7–19.
521 <https://doi.org/10.1007/s10533-009-9297-9>

522 Hoelzle, M., 1992. Permafrost occurrence from BTS measurements and climatic parameters in the Eastern
523 Swiss Alps. *Permafrost Periglac* 3, 143–147. <https://doi.org/10.1002/ppp.3430030212>

524 Hoffmann, U., Hoffmann, T., Johnson, E.A., Kuhn, N.J., 2014. Assessment of variability and uncertainty of
525 soil organic carbon in a mountainous boreal forest (Canadian Rocky Mountains, Alberta). *Catena* 113,
526 107–121. <https://doi.org/10.1016/j.catena.2013.09.009>

527 Islam A.K.M.E., Lotse, E.G., 1986. Quantitative mineralogical analysis of some Bangladesh soils with X-ray,
528 ion exchange and selective dissolution techniques. *Clay Miner.* 21, 31–42.
529 <https://doi.org/10.1180/claymin.1986.021.1.03>

530 IUSS Working Group WRB, 2015. World Reference Base for Soil Resources 2014, update 2015. International
531 soil classification system for naming soils and creating legends for soil maps. World Soil Resources
532 Reports No. 106. FAO, Rome. E-ISBN 978-92-5-108370-3

533 Julián, A., Chueca, J., 2007. Permafrost distribution from BTS measurements (Sierra de Telera, central
534 Pyrenees, Spain): assessing the importance of solar radiation in a mid-elevation shaded mountainous
535 area. *Permafrost Periglac* 18, 137–149. <https://doi.org/10.1002/ppp.576>

536 Karte, J., 1983. Periglacial phenomena and their significance as climatic and edaphic indicators. *GeoJournal*,
537 7(4), 329–340. <https://doi-org.bibliopass.unito.it/10.1007/BF00241455>

538 Kneisel, C., 2006. Assessment of subsurface lithology in mountain environments using 2D resistivity
539 imaging. *Geomorphology*, 80(1-2), 32–44. <https://doi.org/10.1016/j.geomorph.2005.09.012>

540 Kneisel, C., Hauck, C., Fortier, R. and Moorman, B., 2008. Advances in geophysical methods for permafrost
541 investigations. *Permafrost Periglac. Process.*, 19: 157–178. doi:10.1002/ppp.616

542 Knowles, J.F., Blanken, P.D., Lawrence, C.R., Williams, M.W., 2019. Evidence for non-steady-state carbon
543 emissions from snow-scoured alpine tundra. *Nat Commun* 10, 1306. <https://doi.org/10.1038/s41467-019-09149-2>.

544 Léger, E., Dafflon B., Soom, F., Peterson J., Ulrich C., Hubbard, S., 2017. Quantification of Arctic Soil and
545 Permafrost Properties Using Ground-Penetrating Radar and Electrical Resistivity Tomography
546 Datasets, in *IEEE Journal of Selected Topics in Applied Earth Observations and Remote Sensing*, vol.
547 10, no. 10, pp. 4348–4359. doi: 10.1109/JSTARS.2017.2694447

548 Leifeld, J., Zimmermann, M., Fuhrer, J., Conen, F., 2009. Storage and turnover of carbon in grassland soils
549 along an elevation gradient in the Swiss Alps. *Global Change Biology* 15, 668–679.
550 <https://doi.org/10.1111/j.1365-2486.2008.01782.x>

551 Leopold, M., Voelkel, J., Dethier, D., Williams, M., & Caine, N., 2010. Mountain permafrost—a valid archive
552 to study climate change? Examples from the Rocky Mountains Front Range of Colorado, USA. *Nova*
553 *Acta Leopoldina*, 112(384), 281–289.

554 Magnani, A., Viglietti, D., Godone, D., Williams, M.W., Balestrini, R., Freppaz, M., 2017. Interannual
555 Variability of Soil N and C Forms in Response to Snow—Cover duration and Pedoclimatic Conditions
556 in Alpine Tundra, Northwest Italy. *Arctic, Antarctic, and Alpine Research* 49, 227–242.
557 <https://doi.org/10.1657/AAAR0016-037>

558 Mattiolo, E., Novarese, V., Franchi, S., Stella, A., 1951. Carta Geologica D'Italia 1:100000, foglio 29. Istituto
559 Geografico Militare. Firenze, Italy

560 McClymont, A. F., Hayashi, M., Bentley, L. R., Muir, D., Ernst, E., 2010. Groundwater flow and storage within
561 an alpine meadow-talus complex, *Hydrol. Earth Syst. Sci.*, 14, 859–872, <https://doi.org/10.5194/hess-14-859-2010>.

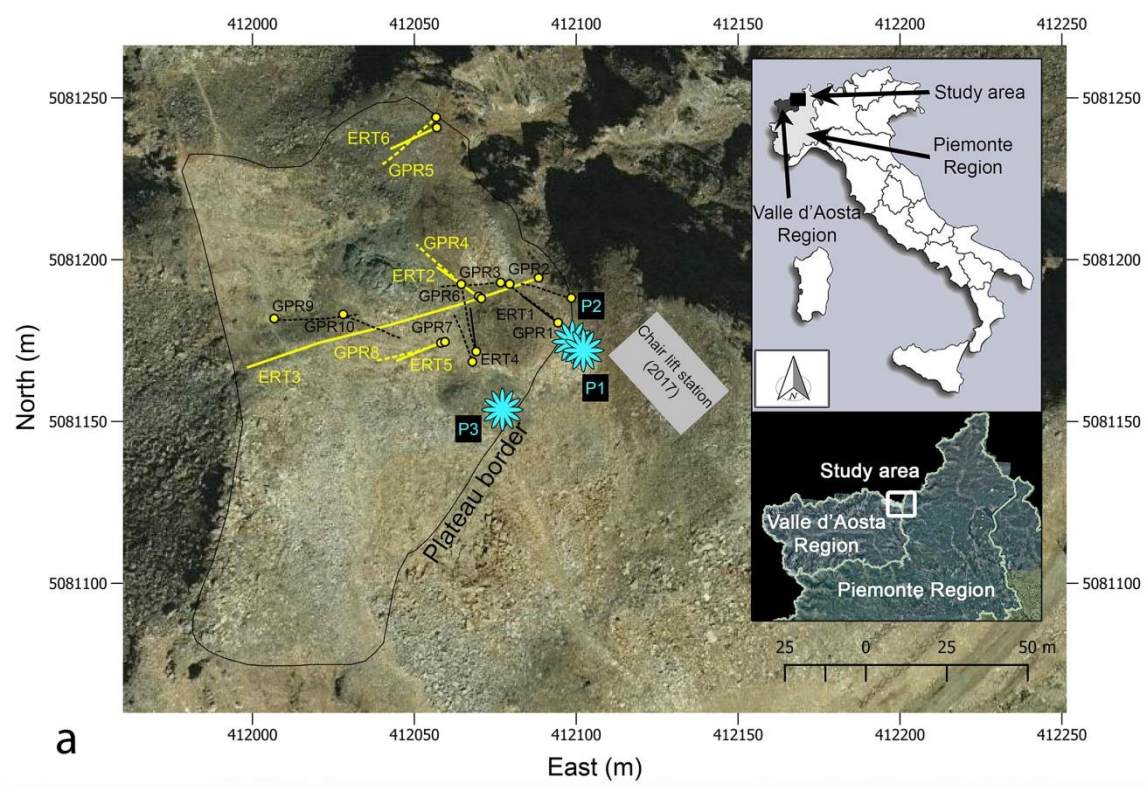
562 Mollaret, C., Hilbich, C., Pellet, C., Flores-Orozco, A., Delaloye, R., Hauck, C., 2019. Mountain permafrost
563 degradation documented through a network of permanent electrical resistivity tomography sites.
564 *The Cryosphere* 13, 2557–2578. <https://doi.org/10.5194/tc-13-2557-2019>

565 Moorman, B. J., Robinson, S., Burgess, M. M., 2003. Imaging periglacial conditions with ground-penetrating
566 radar. *Permafrost and Periglacial Processes* 14 (4), 319–329. <https://doi.org/10.1002/ppp.463>

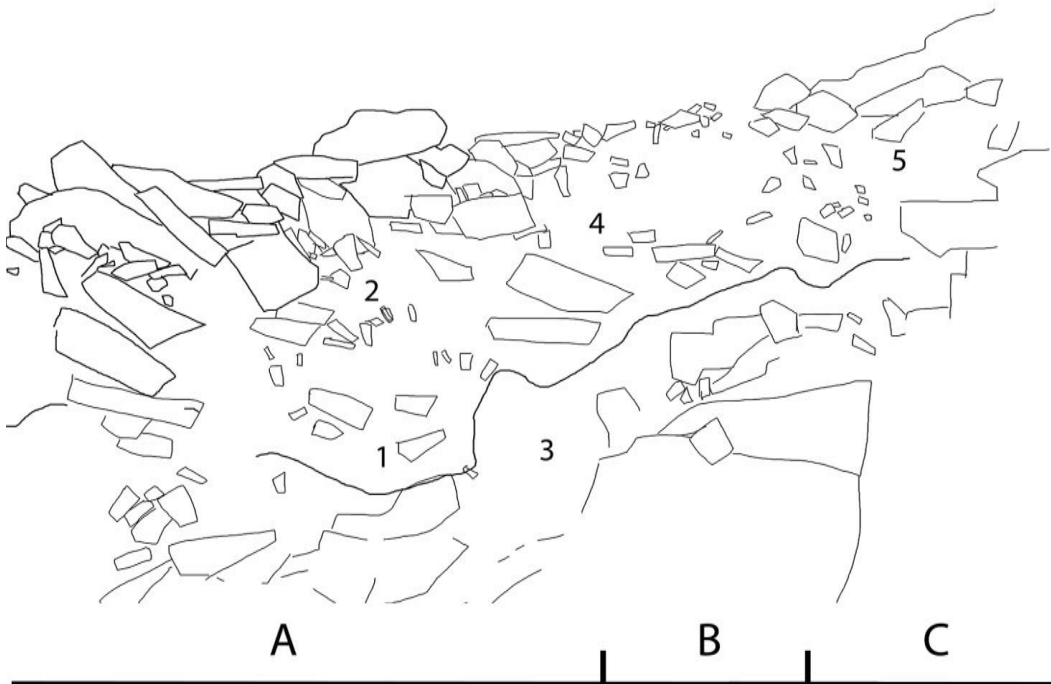
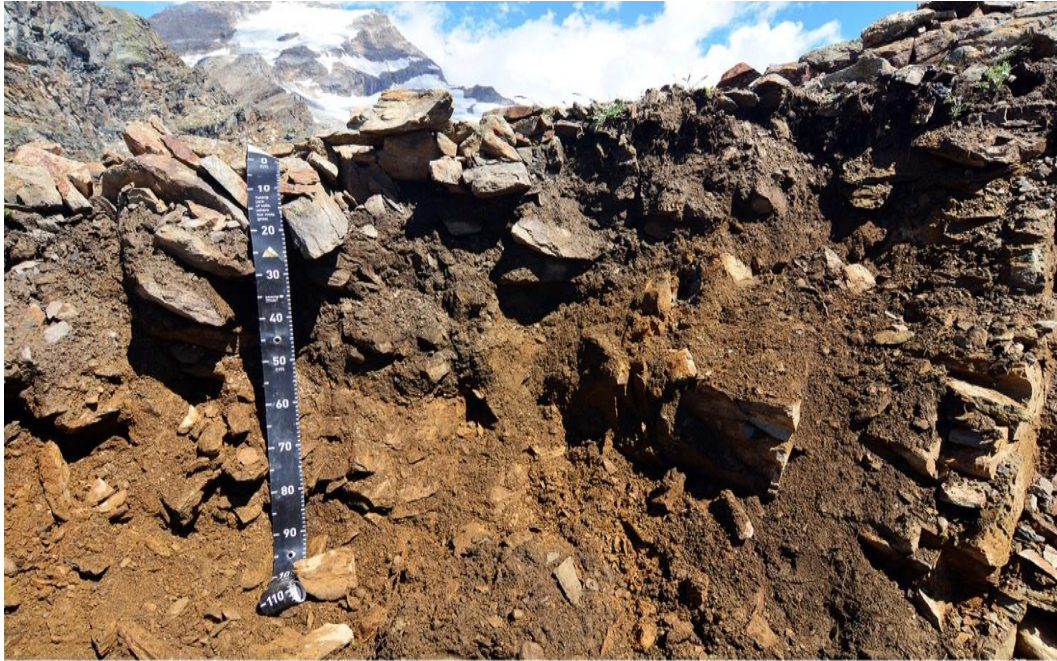
567 Novàková, E., Karous, M., Zajiček, A., Karousová, M., 2013. Evaluation of ground penetrating radar and
568 vertical electrical sounding methods to determine soil horizons and bedrock at the locality Dehtáře.
569 *Soil & Water Res.*, 8 (3), pp. 105–112. <https://doi.org/10.17221/6/2012-SWR>

570 Otto, J.C., Sass, O., 2006. Comparing geophysical methods for talus slope investigations in the Turtmann
571 valley (Swiss Alps), *Geomorphology*, Volume 76, Issues 3–4, 257–272.
572 <https://doi.org/10.1016/j.geomorph.2005.11.008>.

575 Pellet, C., Hilbich, C., Marmy, A., & Hauck, C., 2016. Soil moisture data for the validation of permafrost
 576 models using direct and indirect measurement approaches at three alpine sites. *Frontiers in Earth*
 577 *Science*, 3, 91. <https://doi.org/10.3389/feart.2015.00091>
 578 Samouelian, A., Cousin, I., Tabbagh, A., Bruand, A., Richard, G., 2005. Electrical resistivity survey in soil
 579 science: A review, *Soil Tillage Res.*, 83, 173–193, doi:10.1016/j.still.2004.10.004.
 580 Schuur, E.A.G., Abbott, B.W., Bowden, W.B., Brovkin, V., Camill, P., Canadell, J.G., Chanton, J.P., Chapin,
 581 F.S., Christensen, T.R., Ciais, P., Crosby, B.T., Czimczik, C.I., Grosse, G., Harden, J., Hayes, D.J.,
 582 Hugelius, G., Jastrow, J.D., Jones, J.B., Kleinen, T., Koven, C.D., Krinner, G., Kuhry, P., Lawrence, D.M.,
 583 McGuire, A.D., Natali, S.M., O'Donnell, J.A., Ping, C.L., Riley, W.J., Rinke, A., Romanovsky, V.E., Sannel,
 584 A.B.K., Schädel, C., Schaefer, K., Sky, J., Subin, Z.M., Tarnocai, C., Turetsky, M.R., Waldrop, M.P.,
 585 Walter Anthony, K.M., Wickland, K.P., Wilson, C.J., Zimov, S.A., 2013. Expert assessment of
 586 vulnerability of permafrost carbon to climate change. *Climatic Change* 119, 359–374.
 587 <https://doi.org/10.1007/s10584-013-0730-7>
 588 Smith, M.V., Carrivick J.L., Quincey D.J., 2015. Structure from motion photogrammetry. *Physical Geography*
 589 40, 247–275. <https://doi.org/10.1177/0309133315615805>
 590 Stanchi, S., Freppaz, M., Walter, S., & Vanderwegen, L., 2015. Mountain soils and threats. In *Understanding*
 591 *Mountain Soils: A Contribution from Mountain Areas to the International Year of Soils 2015*; Romeo,
 592 R., Vita, A., Manuelli, S., Zanini, E., Freppaz, M., Stanchi, S., Eds.; FAO: Rome, Italy, 2015; pp. 88–90,
 593 ISBN 978-92-5-108804-3.
 594 Van Reeuwijk, L.P., 2002. Procedures for Soil Analysis. Technical Paper n. 9. ISBN: 90-6672-044-1
 595 Van Vliet-Lanoë, B., 2014. Patterned ground and climate Change. In: Podrovsky, O. (Ed.), *Permafrost:*
 596 *Distribution, Composition and Impacts on Infrastructure and Ecosystems*. Nova Science Publishers,
 597 Inc. chap 2 pp.67–106. (Results of the IPEV CRYOCLIM 2004 program).
 598 Wharton, R.P., Hazen, G.A., Rau, R.A., Best, D.L., 1980. Electromagnetic propagation logging--advances in
 599 technique and interpretation: *Soc. Petr. Eng.*, 55th Annual Technical Conference, Paper 9267.
 600 Wilson, P., 2013. Block/Rock streams. In *Encyclopedia of Quaternary Science*, S.A. Elias, Ed., 3. Elsevier:
 601 Amsterdam; 514–522. DOI: 10.1016/B978-0-444-53643-3.00102-3
 602 Zollinger, B., Alewell, C., Kneisel, C., Meusburger, K., Gärtner, H., Brandová, D., Ivy-Ochs, S., Schmidt,
 603 M.W.I., Egli, M., 2013. Effect of permafrost on the formation of soil organic carbon pools and their
 604 physical-chemical properties in the Eastern Swiss Alps. *CATENA* 110, 70–85.
 605 <https://doi.org/10.1016/j.catena.2013.06.010>
 606



608
609 Figure 1. (a) Location of the study area in the NW Italian Alps (www.pcn.minambiente.it), and overview of the study area
610 (orthoimage Piemonte Region, year 2010); solid and dashed lines indicate ERT and GPR profiles, respectively. Yellow lines
611 indicate the profiles showed and discussed in the manuscript. Yellow circles identify the starting point of each geophysical
612 profile. Cyan polygons indicate the location of the three soil profiles (P1, P2, and P3). (b) View of the plateau (photo by M.
613 D'Amico); dashed lines indicate blockstreams.

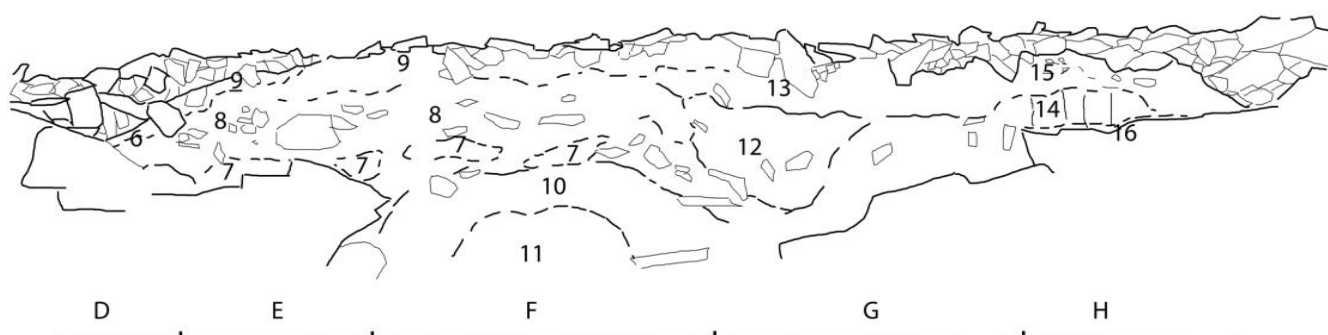
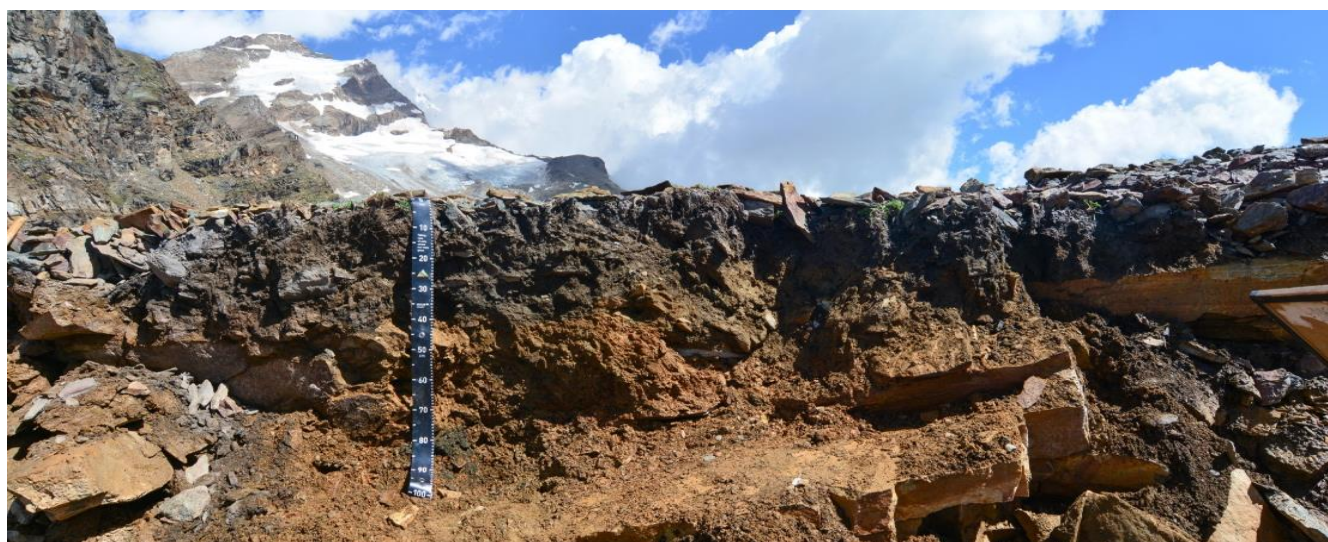


615

616 **Figure 2. Soil profile P1, with the corresponding scheme (below) reporting sampling points (number), the horizon limits (lines**
 617 **therein) and sectors (letters) in which C-stocks were estimated.**

618

619



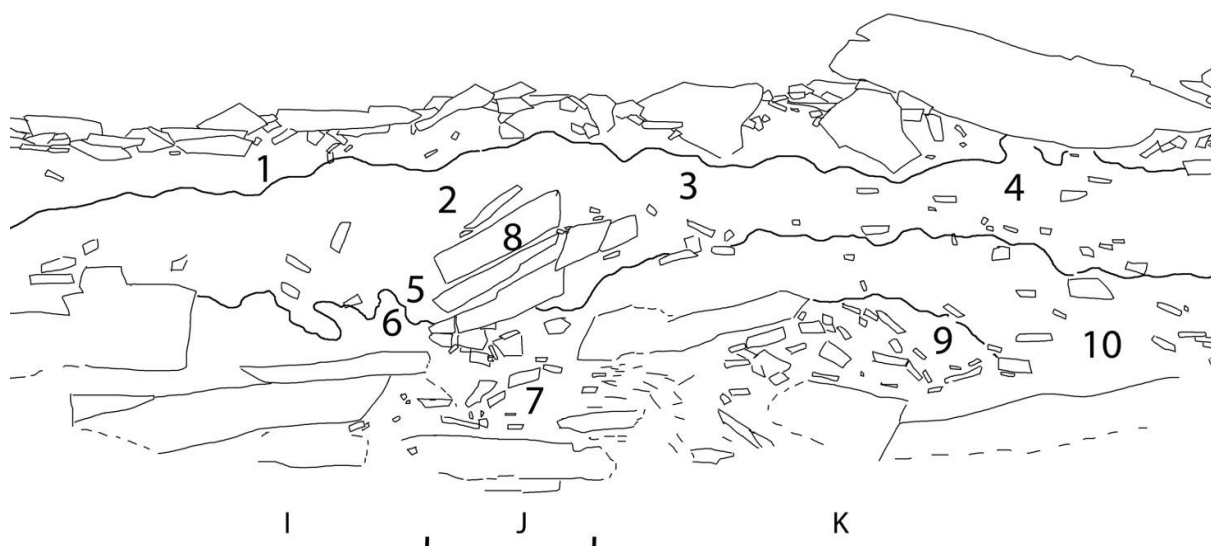
620

621

622

623

Figure 3. Soil profile P2, with the corresponding scheme (below) reporting sampling points (number), the horizon limits (lines therein) and sectors (letters) in which C-stocks were estimated.



624

625 Figure 4. Soil profile P3, with the corresponding scheme (below) reporting sampling points (number), the horizon limits (lines
 626 therein) and sectors (letters I, J, K) in which C-stocks were estimated. Letter "a" indicates blocks dislocated from the rock layer
 627 evidenced by letters "b" and "c", above a deep fracture (wedge); notches in the meter rule indicate 20 cm intervals.

628

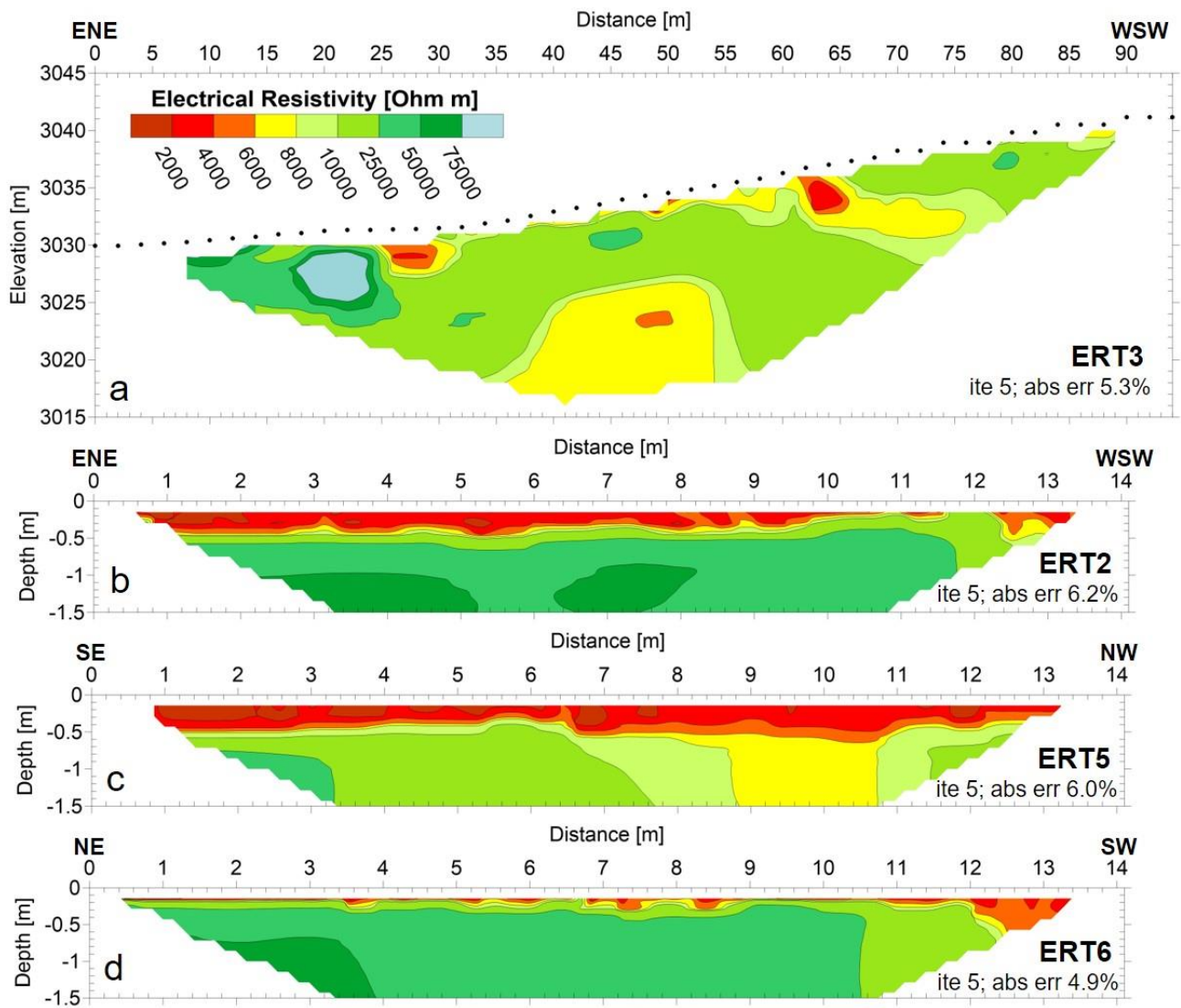
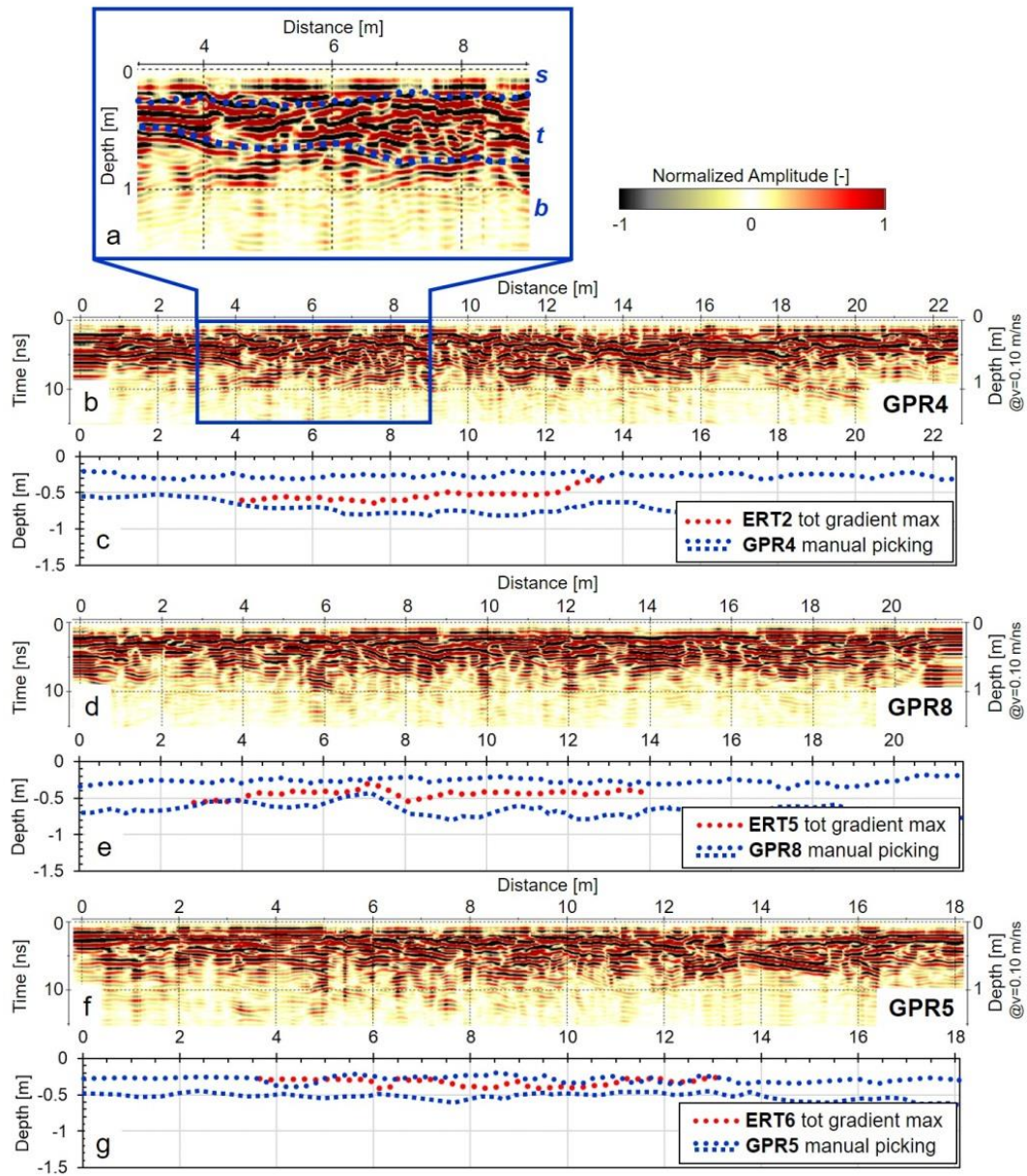


Figure 5. ERT sections: (a) ERT3 (long); (b) ERT2; (c) ERT5; (d) ERT6. The location of the ERT lines is reported in Figure 1. Short sections are cut at 1.5-m depth.



633

634

635

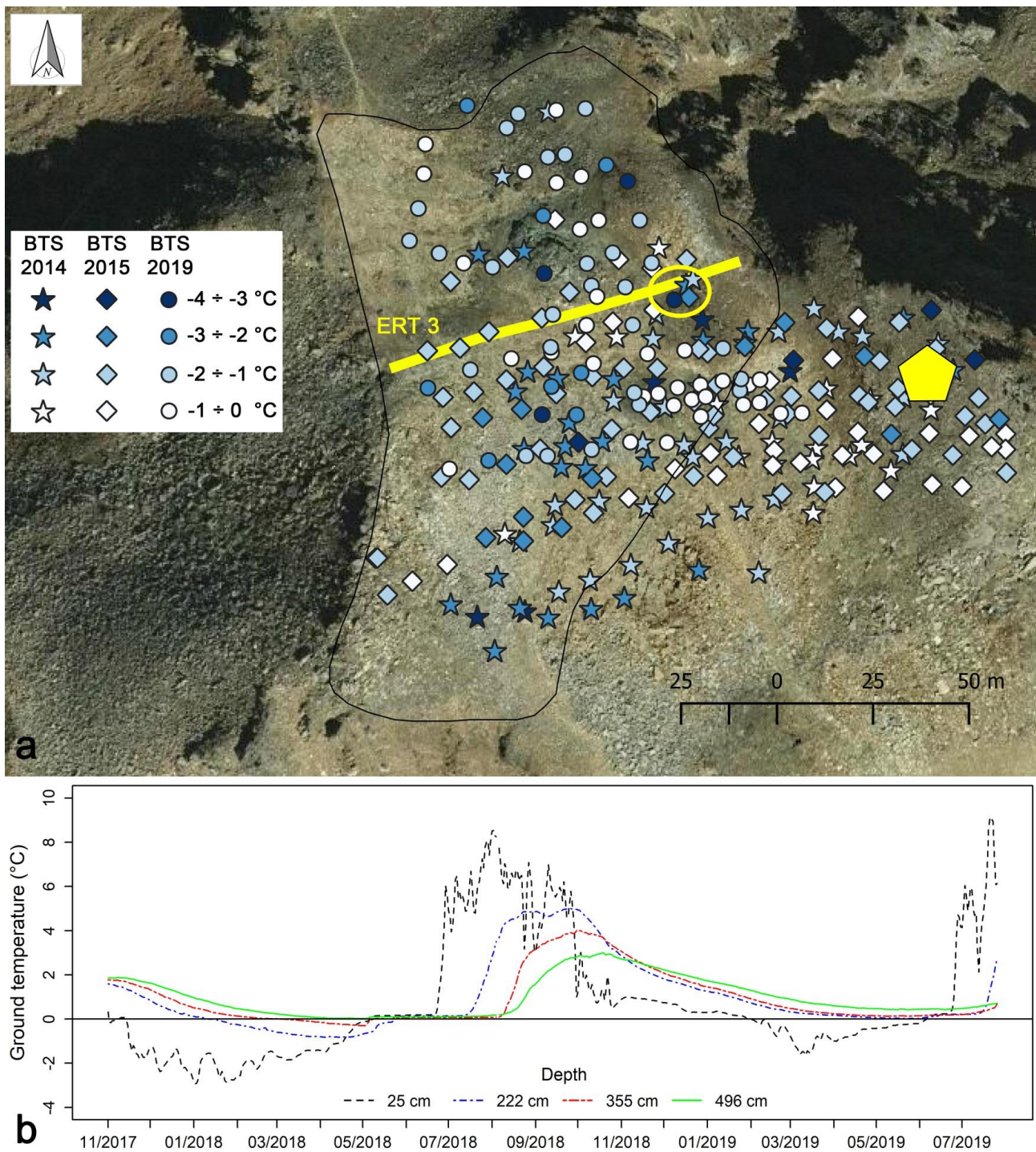
636

637

638

639

Figure 6. GPR sections. (a) Zoom on GPR4 section with tentative interpretation of the shallow stratigraphy: soil (s), soil-to-bedrock transition (t), bedrock (b). (b, d, f) Processed radargrams for lines GPR4, GPR8, GPR5 (vertical cut at 1.5-m depth). (c, e, g) Soil bottom estimation on the above sections. Comparison between the location of the electrical resistivity gradient maxima computed on the ERT lines of Figure 5 (red dots) and the picking of the different layers on GPR results as shown in Figure 6a (in blue, dotted line: s-t interface, dashed line t-b interface). The location of the GPR profiles is reported in Figure 1.



640

641

642

643

644

Figure 7. (a) Location and bottom temperatures of the snow cover (BTS) measurements in 2014, 2015, and 2019. Yellow line represents the ERT3; yellow oval indicates the area of correspondence between a cold spot and the high resistivity body detected by the ERT3; yellow polygon indicates the borehole location for the measurement of ground temperature (GT). (b) GT values measured in the 5-m deep borehole of the station managed by Arpa Piemonte in the northern side of the plateau.

Tables

P1																
Sample number	Horizon	Munsell colour, moist	Stone fragments (%)	Clay (%)	Silt (%)	Sand (%)	Textural class	Structure	pH	TOC (%)	TN (%)	TOC/TN	BD (kg m ⁻³)	TH (m)	VF	C-STOCK (kg m ⁻²)
1	A2	10YR 3/2	30	2.8	14.5	82.7	LS	SB	4.8	1.90	0.10	20	1000	0.20	0.70	2.66
2	A1	10YR 3/2	30	2.5	14.9	82.5	LS	SB	4.4	1.08	0.08	13	1000	0.30	0.70	2.26
3	BA	10YR 3/3	40	1.6	23.3	75.2	LS	BL	4.8	0.47	0.04	11	1200	0.20	0.60	0.68
4	A1+A2	10YR 3/2	40	2.7	15.3	82.0	LS	GR	4.7	1.20	0.10	11	1000	0.30	0.60	2.17
5	A	10YR 3/2	80	2.7	14.5	82.9	LS	GR	4.4	1.86	0.15	13	1000	0.20	0.20	0.74
P2																
6	A	10YR 2/1	30	2.6	20.8	76.5	LS	SB	4.3	0.80	0.08	11	1000	0.20	0.70	1.12
7	A@	10YR 3/2	10	2.3	23.2	74.5	LS	PL/SB	5.6	2.05	0.11	19	1100	0.05	0.90	1.02
8	A2	10YR 3/3	30	1.9	18.3	79.8	LS	SB	4.7	1.10	0.08	14	1000	0.20	0.70	1.53
9	A1	10YR 3/2	70	2.5	12.1	85.4	LS	GR	4.4	1.13	0.11	11	1000	0.10	0.30	0.34
10	BC	10YR 4/4	70	1.4	27.6	71.0	SL	PL/SB	5.3	0.14	BDL	-	1200	0.20	0.30	0.10
11	CB	10YR 5/2	70	1.0	26.3	72.7	LS	SB	5.9	BDL	BDL	-	1200	0.20	0.30	0.00
12	BW	10YR 3/4	60	0.9	25.7	73.4	LS	SB	5.2	0.26	0.03	9	1200	0.20	0.40	0.25
13	A	10YR 3/2	30	4.3	24.1	71.6	SL	BL	4.8	1.09	0.08	14	1000	0.15	0.70	1.15
14	BA	10YR 3/3	50	2.8	29.3	67.9	SL	CO/PR	4.9	1.10	0.07	15	1200	0.20	0.50	1.32
15	A	10YR 3/2	10	3.9	14.0	82.1	LS	GR	4.5	0.71	0.09	8	1000	0.15	0.90	0.96
16	Silt caps	10YR 6/4	10	6.2	41.9	51.9	SL	PL	5.0	0.28	0.03	8	1300	0.03	0.90	0.10
P3																
1	A1	10YR 2/1	70	4.3	8.0	87.7	S	GR	4.9	0.56	0.05	12	1000	0.05	0.30	0.08
2	A2	10YR 3/2	5	3.2	15.6	81.2	LS	GR	4.9	0.87	0.05	17	1000	0.28	0.95	2.28
3	A2	10YR 3/2	5	4.2	15.6	80.1	LS	CO	4.9	1.05	0.07	15	1000	0.25	0.95	2.49
4	A2	10YR 3/2	20	4.8	28.2	66.9	SL	CO	4.8	0.76	0.05	14	1000	0.25	0.80	1.51
5	A2	10YR 3/2	0	4.8	20.7	74.4	SL	SG	4.7	1.18	0.07	17	1000	0.05	1.00	0.59
6	Bw	10YR 5/4	20	2.6	31.8	65.5	SL	SB	5.0	0.15	0.02	7	1200	0.25	0.80	0.35

7	BC	10YR 4/3	50	3.4	16.8	79.9	LS	SB	5.2	0.24	0.02	10	1200	0.20	0.50	0.29
8	A2	10YR 3/2	0	2.8	13.7	83.5	LS	GR	4.9	0.81	0.05	17	1000	0.02	1.00	0.16
9	BC	10YR 4/3	70	4.6	19.5	75.9	LS	PL	5.1	0.31	0.03	9	1200	0.20	0.30	0.22
10	Bw	10YR 3/4	40	3.3	19.6	77.1	LS	SB	5.2	0.16	0.02	8	1200	0.30	0.60	0.36

Table 1. Morphological, physical and chemical properties of the soil samples. Textural class: LS=loamy sand; SL=sandy loam. Structure: SB=subangular blocky; BL=blocky; GR=granular; PL=platy; CO=columnar; PR=prismatic; SG=single grain. BDL=below detection limit.

P1			
Sector	Horizon	Sample number	C-STOCK _{tot} (kg m ⁻²)
A	A1	2	5.18
	A2	1	
	BA	3b	
B	A1+A2	4	2.85
	BA	3	
C	A	5	0.74
P2			
D	A	6	1.12
E	A1	9	2.89
	A2	8	
	A@	7	
F	A1	9	2.99
	A2	8	
	A@	7	
	BC	10	
G	CB	11	1.50
	A	13	
	Bw	12	
H	BC	10b	2.38
	A	15	
	BA	14	
	Silt caps	16	
P3			
I	A1	1	3.30
	A2	2	
	A2	5	
	Bw	6	
J	A1	1	3.02
	A2	3	
	A2	8	
	BC	7	
K	A1	1	2.17
	A2	4	
	Bw	10	
	BC	9	

Table 2. Total C-stock of the profiles for each sector.